PCCP

ROYAL SOCIETY OF CHEMISTRY

PAPER

View Article Online
View Journal | View Issue

Cite this: *Phys. Chem. Chem. Phys.*, 2025, **27**, 9504

Topochemical reduction of FeCo-oxide to FeCo-alloy nanosystems into a SiO_2 matrix†

Jean Pierre Miranda Murillo,[a] Alexander Omelyanchik,[ab] Gianni Barucca,[c] Gaspare Varvaro,[b] Ayda Ghary Haghighat,[bd] Sara Laureti,[b] Aldo Capobianchi,[b] Antonio Comite,[a] Diego Colombara,[a] Nikolaos Ntallis,[e] Kalliopi N. Trohidou,[e] Fabio Canepa,[a] Pierfrancesco Maltoni *[ab] and Davide Peddis *[ab]

Received 22nd January 2025,
Accepted 10th March 2025

DOI: 10.1039/d5cp00305a

rsc.li/pccp

This study focuses on the synthesis of metallic magnetic nanosystems embedded in mesoporous silica (SiO_2), and the impact of matrix porosity, controlled by temperature treatment, on the efficiency of H_2 reduction process. The reduction of FeCo oxides to the corresponding alloy nanosystems was first optimized, identifying FeCo with 50 at% Fe as the optimal composition due to its high saturation magnetization (~242 A m^2 kg^{-1}) and oxidation onset temperature (~440 °C). Then, the FeCo-oxide nanocomposites were synthesized into SiO_2 *via* sol–gel self-combustion under thermal treatments, to properly tune the surface area of the silica matrix. By controlling the annealing temperature, the specific surface area (SA) of the matrix decreases from ~512(1) m^2 g^{-1} to ~345(1) m^2 g^{-1} when annealed to 900 °C in air. Following topochemical reduction in H_2, the structural properties of the obtained FeCo–SiO_2 nanocomposites have been analyzed using X-ray powder diffraction and magnetic properties were evaluated to establish a correlation between matrix SA and reduction capability. The decrease of SA leads to incomplete reduction at higher temperatures, with the formation of Fe_YO_X/Co_XO_Y intermediates. This work underscores the critical role of matrix porosity in achieving a delicate balance to ensure both the efficient conversion of nanostructured oxide to their metallic state and the preservation of their magnetic and structural integrity.

Introduction

The synthesis of nanostructured FeCo alloys has attracted considerable interest due to their soft magnetic properties (*i.e.*, low coercivity H_c, high magnetic moment and large magnetic susceptibility) compared to their oxide counterparts.[1,2] Technological applications demand a large magnetic energy density and the ability to operate at both large magnetic fields and high frequencies, thus requiring a large magnetic moment and a high Curie temperature.[3–6] This applies to several sectors such as medical,[7] power conversion,[8,9] media recording,[10] and catalysis,[11,12] owing to the number of techniques that can allow the preparation of nanosystems with various morphologies.[13–15] FeCo-alloys can be integrated into multiple matrices or substrates to create composite materials with enhanced functionalities.[16–18]

The FeCo-alloy is a ferromagnetic system with a saturation magnetization, M_s, which may reach up to ~245 A m^2 kg^{-1} at 300 K, the highest value among binary alloys. This is more than twice that of common bulk oxides ferrimagnetic iron oxides (*e.g.*, maghemite, γ-Fe_2O_3, M_s = 72 A m^2 kg^{-1} and magnetite, Fe_3O_4, M_s = 83 A m^2 kg^{-1}) or cobalt ferrite ($CoFe_2O_4$, M_s = 80 A m^2 kg^{-1}).[19–24] Furthermore, it has a high Curie temperature T_c up to ~1200 K. However, these metallic systems at the nanoscale face challenges such as chemical instability and oxidation.[25] Typically, these issues have been addressed by encapsulating the particles within protective matrices, with amorphous silica (SiO_2) being a commonly employed material.[26–31] Recently, metal-embedded silica nanostructures have attracted considerable attention as biocompatible and stable templates, particularly for embedding noble metals.[32] While the reduction of oxide nanosystems within these matrices, often carried out by hydrogen (H_2) treatment during sintering, is well-established, the role of matrix textural

[a] *Department of Chemistry and Industrial Chemistry & INSTM RU, University of Genoa, 16146 Genoa, Italy. E-mail: pierfrancesco.maltoni@unige.it davide.peddis@unige.it*
[b] *Institute of Structure of Matter, National Research Council, nM2-Lab, Via Salaria km 29.300, Monterotondo Scalo 00015, Rome, Italy*
[c] *Department of Science and Engineering of Matter, Environment and Urban Planning, University Politecnica delle Marche, Via Brecce Bianche 12, 60131 Ancona, Italy*
[d] *Department of Science, University of Roma Tre, Via della Vasca Navale 84, 00146, Rome, Italy*
[e] *Institute of Nanoscience and Nanotechnology, NCSR "Demokritos", Agia Paraskevi, Attiki 153 10, Greece*

† Electronic supplementary information (ESI) available. See DOI: https://doi.org/10.1039/d5cp00305a

properties (*i.e.* surface area) in this process has been overlooked in the literature. The permeation of H_2 driving the reduction of oxide nanoparticles depends on the thickness and porosity of the silica matrix, but also on the reaction conditions (annealing temperature and H_2 flow).[33–35] The reported reduction temperature is usually very high, in the 600–900 °C range,[36–40] which is not only energy consuming, but may also generate by-products such as fayalite (Fe_2SiO_4),[26] that deteriorate the magnetic properties.

This study aims to fill this gap by systematically investigating the influence of matrix porosity, controlled through the thermal treatment, on the efficacy of topochemical H_2 reduction of nanostructured oxide with spinel structure to metal alloys. The study focuses on nanocomposites of FeCo-oxides in mesoporous silica synthesized *via* sol–gel self-combustion, with thermal treatment selectively altering the surface area of the silica matrix. By controlling matrix porosity, we demonstrated that the reduction process is driven by the textural features of the matrix controlling the diffusion of H_2 and the conversion of oxide particles to their metallic form. Through this work, we highlight the critical role of matrix porosity in facilitating solid-state chemical transformation due to H_2 access. Overall, our findings underscore the importance of balancing matrix porosity to ensure both efficient conversion of oxide nano-systems to metallic states and preservation of their magnetic and structural integrity.

Experimental

FeCo-oxides and alloys

The synthesis of FeCo-oxides and FeCo-alloys followed procedures outlined in previous studies,[41] with detailed information provided in the ESI.† In summary, $Fe(NO_3)_3{\cdot}9H_2O$ (Sigma Aldrich, 98%) and $Co(NO_3)_2{\cdot}6H_2O$ (Sigma Aldrich, 98%) were dissolved in deionized water in the desired ratio, and $C_6H_8O_7$ (citric acid, Sigma Aldrich, 99.5%) was introduced as a chelating agent.[42] The ratio of metallic ions was carefully selected to adjust the Fe^{3+} at% in the final oxide, ensuring that Fe^{3+} at% + Co^{2+} at% equaled 100 (with Fe^{3+} at% varying as 100, 67, 50, 33, or 0). Following adjustment of the pH to 7 using NH_4OH (ammonia solution 30% (aq.), Sigma Aldrich), the solution was dried to form a thick gel, which was subsequently heated to induce crystallization, yielding FeCo-oxides powders.

These powders underwent grinding and annealing in a hydrogen (H_2) flow environment (83% H_2 in N_2, flow rate of 65 mL min^{-1}) for 5 hours at 500 °C to obtain metal particles.

FeCo-oxides in SiO_2

Nanocomposites of FeCo-oxides in silica with a silica content of 70 wt% were synthesized by following a procedure similar to that outlined by Cannas *et al.*[43] Initially, 5 mmol of $Fe(NO_3)_3{\cdot}9H_2O$ and 5 mmol of $Co(NO_3)_2{\cdot}6H_2O$ were dissolved in 23 mL of deionized water along with 10 mmol of citric acid in a Teflon beaker under magnetic stirring. The molar concentration ratios were carefully adjusted, with both Fe^{3+}/Co^{2+} and $(Co^{2+} + Fe^{3+})$/citric acid set to 1, resulting in a total molar concentration in water ($Co^{2+} + Fe^{3+}$ + citric acid) of 1. The pH of the solution was then adjusted to 2 by adding NH_4OH (30% water solution) dropwise. Subsequently, tetraethyl orthosilicate (TEOS, Sigma Aldrich, 98%) was dissolved in approximately 45 mL of absolute ethanol, and this solution was added to the nitrate solution in water. The pH was once again adjusted to 2, and the mixture was stirred for 40 minutes at room temperature. The resulting solution was then allowed to dry in a preheated oven set at 40 °C for 24 hours. The dried gel obtained was transferred to a pyrex beaker and heated on a hot plate set to 350 °C. After a short time, the gel underwent self-combustion, yielding a black powder. This powder was subsequently ground using an agate mortar, and annealed in air at different temperatures, reported in Table 1. The oxide samples were denoted as NCFO_*X*00 (N = nanocomposite, C = cobalt, F = iron, O = oxygen), with the subscript *X*00 indicating the annealing temperature in air (*X*00 °C with *X* = 3, 5, 7, 9).

Table 1 List of samples and corresponding annealing details

Sample name	Precursor	Temperature (°C)	Time (h)	Atmosphere
NCFO		Post synthesis		
NCFO_300	NCFO	300	1	Air
NCFO_500	NCFO	500	1	Air
NCFO_700	NCFO	700	1	Air
NCFO_900	NCFO	900	1	Air
NCF_300	NCFO_300	500	5	H_2/N_2
NCF_500	NCFO_500	500	5	H_2/N_2
NCF_700	NCFO_700	500	5	H_2/N_2
NCF_900	NCFO_900	500	5	H_2/N_2

FeCo-alloys in SiO_2

NCFO_*X*00 oxide samples underwent reduction under identical annealing conditions, specifically with a flow rate of 65 mL min^{-1} of 83% H_2 – 17% N_2 for 5 hours at 500 °C (Table 1). The corresponding reduced samples were labelled as NCF_*X*00. To prevent oxidation, the samples were stored inside an Ar-filled glove box.

Methods

X-ray powder diffraction (XRPD) was conducted with a MiniFlex (Rigaku) X-ray diffractometer equipped with a Cu K_α anode (λ = 1.54184 Å) in the 2θ geometry using a step size of 0.01° and 1 second per step. Phase identification was performed by comparison with literature patterns using the Pearson Crystal Database. The average size of the crystallites was extracted from Scherrer equation.[44] The lattice constant of cubic phases was calculated using equation $a = d_{HKL}\sqrt{h^2 + k^2 + l^2}$. It should be underlined that all the XRD patterns reported in this paper contain a strong background due to the presence of amorphous silica. In this scenario, both crystallite size and lattice constant should be considered as a rough estimation. Transmission electron microscopy (TEM) images were acquired using a Philips CM200 microscope operating at 200 kV and equipped with a LaB_6 filament. The differential thermal analysis and thermogravimetry (DTA/TG) were performed by using a Labsys Evo 1600 Setaram between 25 and 1000 °C. The surface area

(SA) of the samples was calculated using an ASAP 2020 Plus MP, Micromeritics, USA, with the Brunauer–Emmett–Teller (BET) method at 300 K. Inductively coupled plasma – atomic emission spectroscopy (ICP-AES) measurements were performed using an iCAP 6300 DUP ICP-AES spectrometer (ThermoScientific) to check the composition of each sample.

Field-dependent magnetization loops (*M vs. H*) were recorded at 300 K using a Model 10 Microsense Vibrating Sample Magnetometer (VSM) equipped with an electromagnet producing a maximum magnetic field of 2 T.

Results and discussion

FeCo-oxides and alloys

Five different metallic samples (with Fe at% varying as 100, 67, 50, 33, and 0) were prepared by reduction in H_2 of the corresponding FeCo-oxides powders, previously obtained by sol–gel self-combustion method. Fig. 1 shows the patterns for the starting oxides and the corresponding reduced metal particles, revealing the complete reduction (*i.e.*, absence of oxide phases) achieved under the explored annealing conditions (see Table 1).

The synthetized oxides are predominantly composed of cubic spinel ferrite phase ($Fd\bar{3}m$ space group). Upon reduction, the samples underwent a significant structural transformation. The XRPD patterns of the reduced samples reveal characteristic reflections corresponding to a body-centered cubic (bcc) structure, which is typical for FeCo alloys with $Pm\bar{3}m$ space group.[45] This bcc structure was observed across the composition range, with two notable exceptions: the pure iron ($Im\bar{3}m$) and the pure cobalt sample. In the case of pure Co, the XRPD pattern was indexed to a face-centered cubic (fcc) structure belonging to the $Fd\bar{3}m$ space group. The lattice constant a decreases gradually from 2.870(1) Å for pure Fe to 2.845(1) Å for FeCo with 33 at% of Fe as expected for FeCo alloys with more than 20% cobalt content.[46] For pure Co, the lattice constant (3.547(1) Å) is close to the values reported earlier for fcc $Co^{(0)}$ nanoparticles.[45] The crystal size $\langle D \rangle$ of all metal nanoparticles is around 30 nm. As expected, all metallic particles exhibit a higher saturation magnetization (M_s), as extracted from the magnetic hysteresis loops reported in ESI† (Fig. S1 and S2), compared to the starting oxide particles (Fig. 2), with a maximum value for the FeCo-alloys with Fe at% of 50 and 67. The observed values, also

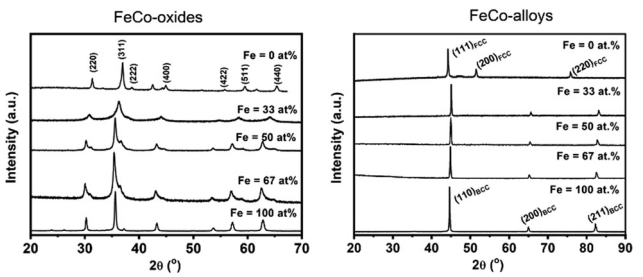

Fig. 1 XRPD patterns of the nanostructured FeCo-oxides before (left) and after (right) the reduction process in H_2.

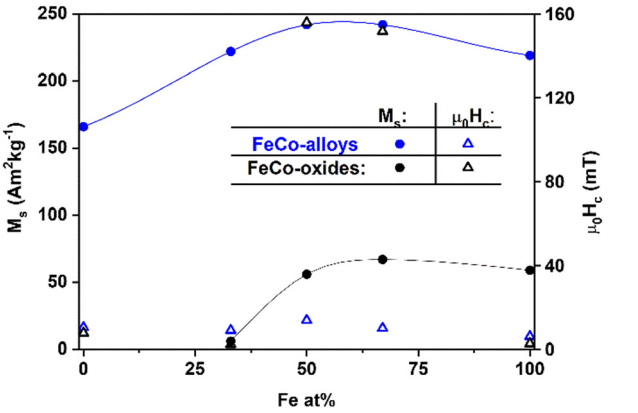

Fig. 2 Saturation magnetization, M_S, and coercivity, μ_0H_c, of different samples of nanostructured FeCo-oxides before (black dots) and after (blue dots) the reduction process in H_2 atmosphere.

reported in Table 2, closely align with the theoretical M_s for those FeCo compositions,[19,47] also predicted by DFT calculations,[48,49] which highlights the maximum of the saturation magnetization in the region of 35–50 Co at% for systems above 20 nm in size (see ESI,† for more details, Fig. S3) closer to bulk values,[50] confirming the effective reduction within the used conditions.

Then, to assess the stability of the obtained alloys against oxidation, TG experiments were conducted (see Fig. S4 in ESI,† for TG analysis). Particularly, the onset temperature of oxidation for FeCo with 50 at% of Fe was found at ~440 °C, relatively higher than that for other compositions, suggesting its suitability for applications requiring higher thermal stability and oxidation resistance. Considering also the notable M_s value, this alloy was chosen as a model sample for investigating the structural and magnetic properties when it is embedded in a silica matrix.

FeCo-oxides and alloys in SiO_2

At first, a sample of FeCo-oxide in SiO_2 30/70 wt%, denoted as NCFO, was prepared with a synthetic approach integrating traditional sol–gel techniques, involving the hydrolysis and condensation of alkoxide precursors, with nitrate–citrate sol–gel self-combustion.[43] This procedure has successfully yielded nanoparticles consisting of $CoFe_2O_4/Co_3O_4$ spinel phases (due to the Co : Fe 1 : 1 ratio[51]), dispersed within an amorphous silica matrix. The XRPD patterns for the NCFO samples are reported in Fig. 3. Only the (311) reflection of the $Fd\bar{3}m$ space group of the main spinel $CoFe_2O_4$ phase appears in the pattern of the NCFO

Table 2 Saturation magnetization (M_S), coercivity, (μ_0H_C), average crystallite size ($\langle D \rangle$), and lattice constant (a) of the samples after reduction of FeCo-oxide particles at 500 °C for 5 h in a H_2 flow

Fe (at%)	Fe (at%) [ICP-AES]	M_s (A m^2 kg^{-1})	μ_0H_c (mT)	$\langle D \rangle$ (nm)	a (Å)
100		219(4)	6(1)	31(6)	2.870(1)
67	62.8(6)	242(6)	10(1)	29(4)	2.861(1)
50	45.4(5)	242(5)	14(1)	29(3)	2.854(1)
33	29.7(3)	222(1)	9(1)	33(6)	2.845(1)
0		166(4)	10(1)	30(4)	3.547(1)

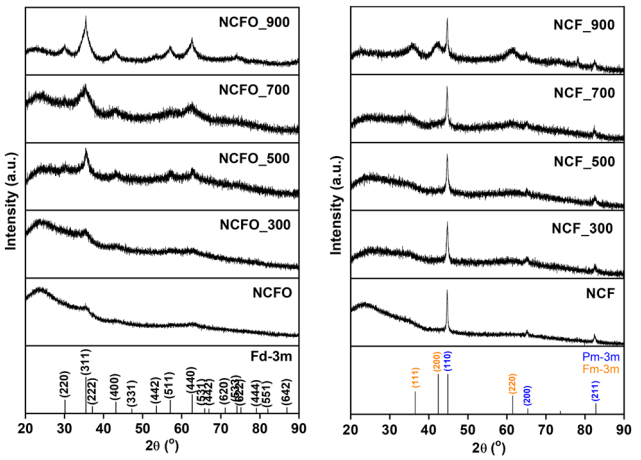

Fig. 3 (Left) XRPD patterns of the samples obtained by the sol–gel self-combustion synthesis and after thermal treatment at 300 °C, 500 °C, 700 °C, and 900 °C for 1 h in air. (Right) corresponding XRPD patterns after treatment in H_2 at 500 °C for 5 h.

nanocomposite, whereas the other expected reflections are hidden by the amorphous silica matrix (70 wt%), whose hump is visible between 20°–30° (Fig. 3). The predominance of this spinel phase becomes more conspicuous following annealing up to 900 °C, attributed to growth and possibly potential reorientation of the initial particles. However, the average crystallite size remains relatively small (<7 nm) due to the constraining effect of the silica matrix, which prevents significant particle growth.[52] The confirmed high porosity of the matrix for NCFO, as indicated by BET analysis in Table 3, diminishes post-annealing in air, from 512 $m^2\ g^{-1}$ for NFO to 345 $m^2\ g^{-1}$ for NCFO_900 (∼30%), implying that the lower SA will potentially affect the subsequent reduction process making it less effective.[33–35]

The composites annealed at several temperatures were then treated in a reducing H_2 atmosphere at 500 °C. XRPD patterns of the reduced NCF samples reveal distinct reflections at 2θ = 44.7, 65.2, and 82.4°, corresponding to the $Pm\bar{3}m$ spacegroup of the FeCo alloy with 50 Fe at%, validating the successful reduction to the metallic alloy phase (up to NCF_500). Nonetheless, additional reflections were observed in the XRPD patterns of samples NCF_700 and NCF_900 at 2θ ∼36.3, ∼42.0, ∼61.7, and ∼78.1°, suggesting the presence of intermediate phases such as Fe or Co monoxides (FeO and CoO, respectively) or a spinel $(Fe_{1-x}Co_x)_3O_4$ phase, possibly arising from incomplete reduction attributed to increased particle size, and decreased SA. Additionally, the estimated crystallite size of the alloy nanocomposites remains quite constant across the series independently of the thermal treatment in H_2 (see Table 4). This lack of dependence is presumably due to the silica matrix and its confinement effect, which however makes the size estimation not trivial due to the amorphous contribution in the pattern. TEM images (see Fig. 4) offer valuable insights into the morphology of both pure FeCo-alloy particles and their corresponding nanocomposites.

Table 3 Iron content (Fe at%), specific surface area (SA), and average pore size for NCFO, NCFO_500 and NCFO_900 samples

Sample name	Fe (at%)	SA ($m^2\ g^{-1}$)	Av. pore size (nm)
NCFO	55(3)	512(8)	5(1)
NCFO_500	55(3)	413 (7)	5(1)
NCFO_900	55(3)	345(5)	4(1)

Table 4 Average crystallite size (⟨D⟩) and lattice parameter (a) of the FeCo-oxides (NCFO) and FeCo-alloys (NCF)

	NCFO		NCF	
Annealing X00 °C	⟨D⟩ (nm)	a (nm)	⟨D⟩ (nm)	a (Å)
Post synthesis	n.d.	n.d.	23(5)	2.865(11)
300	n.d.	n.d.	15(4)	2.841(13)
500	5(3)	8.38(6)	19(3)	2.840(11)
700	4(3)	8.50(6)	20(2)	2.875(6)
900	7(3)	8.41(7)	23(6)	2.867(7)

FeCo-alloy grains have irregular shapes with sizes ranging from 50 to 400 nm (Fig. 4a) and are interconnected giving rise to highly porous structures. The inherently high porosity observed in the FeCo-alloy validates the selection of this material as the ideal starting system for this topochemical reduction process. When the silica matrix is added to form the nanocomposites, the FeCo-alloy grains are trapped inside the porous amorphous matrix. Fig. 4b shows a typical cluster of FeCo-alloy grains (dark arrows) inside a finely porous amorphous matrix (for sample NCF). In principle, the abundant active sites provided by the finely dispersed nanophase within this structurally open matrix should enhance diffusion kinetics and catalytic activity.[53,54] The same trend was confirmed for the set of samples in Table 1. In particular, when NCFO is annealed at higher temperatures, ferrite particles crystallise while remaining confined in the matrix, Fig. 5a. Selected area electron diffraction (SAED) measurements were performed (inset of Fig. 5a). All the visible diffraction rings can be attributed to the cobalt ferrite phase, suggesting that the Co_3O_4 phase, if present, is poorly crystallised. TEM dark-field images were performed to evidence the crystallites in the amorphous matrix. Fig. 5b was obtained with the diffraction spots encircled in the SAED image of Fig. 5a's inset and the crystallites corresponding to those diffraction spots appear brighter in the image. The subsequent reduction process yields the expected

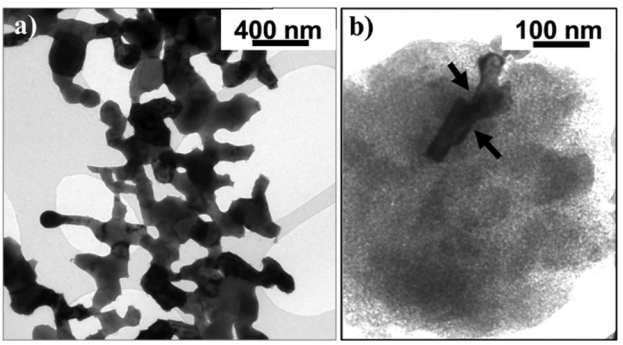

Fig. 4 TEM images of the CoFe-alloy with 50 at% (left, (a)) and the CoFe-alloy/SiO_2 (NCF) composite (right, (b) obtained by the NCFO sample reduction.

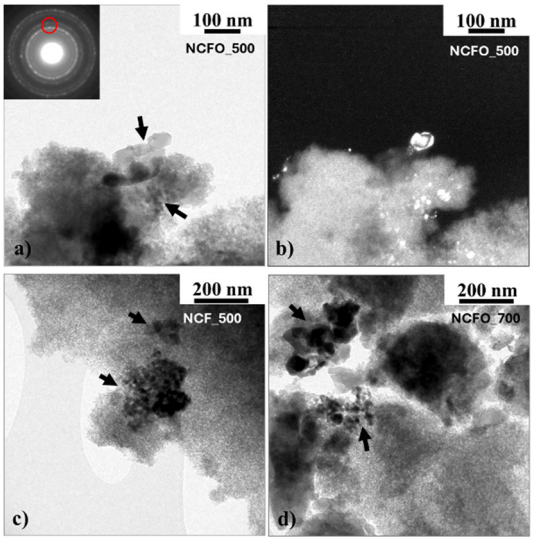

Fig. 5 (a) Bright-field TEM image showing the crystalline phase (arrows) inside the silica amorphous matrix. The inset is a typical selected area electron diffraction (SAED) pattern taken on a large sample area. (b) Corresponding dark-field image obtained with the diffraction spots circled in (a) insetM (c) bright-field TEM image showing the reduced crystalline phase (arrows) inside the silica amorphous matrix. (d) Bright-field TEM image of the sample NCFO_700: the crystallites inside the silica amorphous matrix are indicated by arrows.

FeCo phase (NCF_500 in Fig. 5c), without changing the morphology of the composite. If we consider a higher annealing temperature in air, as shown for NCFO_700 in Fig. 5d, we did not observe relevant changes, in agreement with the results from XRPD analysis.

Further details about the reduction process can be obtained from field-dependence magnetization loops at 300 K (see Fig. 6). The composite NCFO_900 shows an increase of both M_s and $\mu_0 H_c$ from ~5 to 12 A m^2 kg^{-1} and from ~8 to 21 mT, respectively, when annealed in air at 900 °C for 1 h. This behavior can be ascribed to the particle's crystallization and consequent growth inside the matrix compared to NCFO.[55] After the reduction process (Fig. 6 right), the M_s of the NCF sample increases from ~5 to 60 A m^2 kg^{-1}, specifically by ~12 times compared to NCFO, consistently with the transformation in FeCo-alloy. The measured coercivity (~40 mT) is a bit higher to what is expected for the FeCo alloy, suggesting an incomplete reduction of the sample or the existence of a thin passive layer. This was also observed in previous studies, where

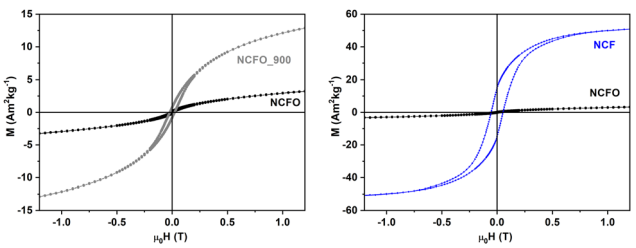

Fig. 6 Magnetization (*M*) *vs.* applied field (*H*) at 300 K for NCFO/NCFO_900 (left), and NCF/NCFO (right).

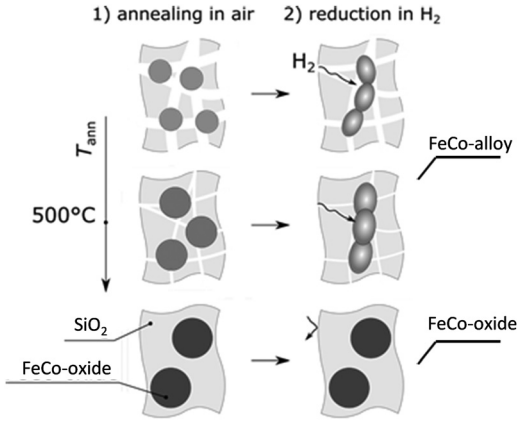

Fig. 7 Schematic representation of the annealing process.

they show possible passivation of the alloy inside the matrix.[36] On the other hand, the pattern of NCF_900 reveals a mixture of phases, making the comparison complex: this is presumably due to the presence of Fe_YO_X/Co_XO_Y and Co ferrite as the FeCo alloy is probably obtained in low yield or rich in iron,[45] because of the much lower SA of NCF_900.

Our investigations demonstrate that annealing in air before reduction critically influences the matrix porosity, directly impacting hydrogen diffusion and, consequently, the efficiency of oxide-to-alloy conversion (see the scheme of Fig. 7). This, in turn, determines the final magnetic properties of the embedded nanoparticles, with higher annealing temperatures leading to incomplete reduction and lower saturation magnetization.

To corroborate and expand the applicability and effectiveness of the method, we applied the reducing treatment to a composite, referred to as NFO, having the same composition in

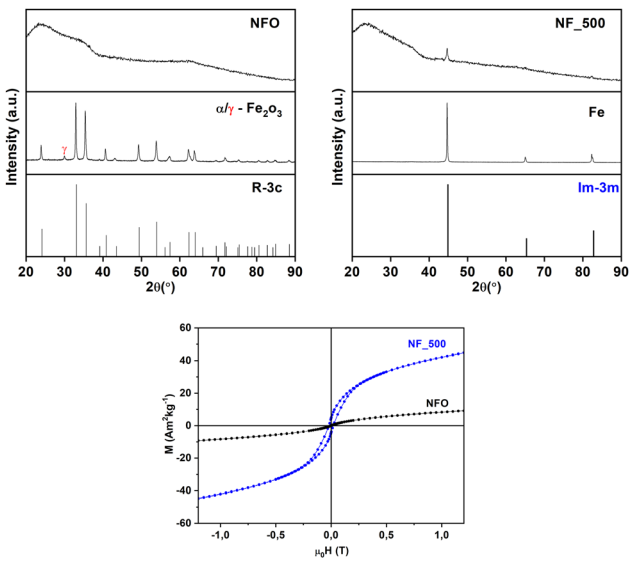

Fig. 8 XRPD patterns of the iron-based samples obtained by the sol–gel self-combustion synthesis (top, left) and after thermal treatment in H_2 (top, right). Field dependence of magnetization at 300 K for NFO and NF_500 samples (bottom).

silica and iron oxides (*i.e.*, a mixture of maghemite/hematite), as shown in Fig. 8. The results suggest a complete reduction of the oxide phases (right panel) to Iron $Im\bar{3}m$ (left panel), wherein the reflections corresponding to the oxides disappear as previously observed for the oxide phases without silica matrix. The emergence of the metallic phase is accompanied by the enhancement of M_s visible in the hysteresis loop in the bottom panel of Fig. 8, and thus confirming the reproducibility of the reducing treatment on composites of different spinel oxides phases embedded in a porous silica matrix.

Conclusions

This study highlights the role of matrix porosity and thermal treatment in governing the topochemical reduction of oxides to metal alloys. By tuning the surface area through annealing, we controlled the diffusion of H_2, which directly impacts the extent of reduction and the resulting magnetic properties. When the specific surface area of the matrix decreases due to high-temperature annealing (from $\sim$512 m^2 g^{-1} post-synthesis, to $\sim$413 m^2 g^{-1} at 500 °C and finally to $\sim$345 m^2 g^{-1} at 900 °C), the reduction becomes incomplete, as the limited porosity restricts hydrogen penetration, preventing the full conversion of the oxide phase. This effect is particularly evident in samples annealed above 900 °C, where metallic alloy formation is hindered, and residual spinel oxide phases persist, leading to lower M_s ($\sim$80%) in response to the $\sim$30% decrease in SA.

Author contributions

J. M., A. O., P. M., F. C. and D. P. designed the experiments; P. M., A. O. and D. P. coordinated the data analysis and discussion. J. M. and A. G. synthesized the nanoparticles and characterized them by XRPD and magnetometry techniques, whose results were discussed with G. V., S. L. and D. C. G. B. performed structural characterization by TEM. A. C. performed BET analysis. D. P. acquired the funding, designed and supervised the whole activity. All authors contributed to the results, discussion, and revision of the article.

Data availability

Data will be made available on request.

Conflicts of interest

The authors declare that they have no known competing financial interests or personal relationships that could have appeared to influence the work reported in this paper.

Acknowledgements

This work was partially developed in the framework of the PRIN 2022-PNRR project HyperMag (prot. P2022RRRT4) and supported by European Union – NextGenerationEU. D. P. acknowledges project code PE0000021, Concession Decree No. 1561 of 11.10.2022 adopted by the ''Ministero dell'Università e della Ricerca (MUR)'', according to attachment E of Decree No. 1561/2022, Project title ''Network 4 Energy Sustainable Transition-NEST'' in the frame of a study on surface wettability properties, and REMAP, which has received funding from the European Commission PathFinder Open programme under grant agreement No. 101046909. Funded by the European Union. Views and opinions expressed are however those of the author(s) only and do not necessarily reflect those of the European Union or European Innovation Council and SME Executive Agency (EISMEA). Neither the European Union nor the granting authority can be held responsible for them.

References

1 J. M. Silveyra, E. Ferrara, D. L. Huber and T. C. Monson, *Science*, 2018, **362**(6413), DOI: 10.1126/science.aao0195.
2 J. M. D. Coey, *Magnetism and Magnetic Materials*, Cambridge University Press, 2001.
3 C. Desvaux, C. Amiens, P. Fejes, P. Renaud, M. Respaud, P. Lecante, E. Snoeck and B. Chaudret, *Nat. Mater.*, 2005, **4**, 2–5.
4 D. L. Huber, *Small*, 2005, **1**, 482–501.
5 J. Liu, D. Su, J. Wang and K. Wu, *J. Nanopart. Res.*, 2020, **22**, 1–16.
6 G. Reiss and A. Hütten, *Nat. Mater.*, 2005, **4**, 725–726.
7 Ö. Çelik and T. Fırat, *J. Magn. Magn. Mater.*, 2018, **456**, 11–16.
8 H. Lewis and L. F. Jimenez-Villacorta, *Metall. Mater. Trans. A*, 2013, **44A**, 1–20.
9 C. J. Guzman-Minguez, S. Ruiz-Gomes, M. L. Vicente-Arche, C. Granados-Miralles, C. Fernandez-Fonzalez, F. Mompean, M. Garcia-Hernandez, S. Erohkin, D. Berkov, D. Mishra, C. Julian Fernandez, F. Fernandez, J. L. Perez and A. Quesada, *ACS Appl. Nano Mater.*, 2020, **3**, 9842–9851.
10 T. Burkert, O. Nordstrom, L. Eriksson and O. Heinonen, *Phys. Rev. Lett.*, 2004, **1**, 1–4.
11 Z. Liang, T. Qi, H. Lui, L. Wang and Q. Li, *Sci. Total Environ*, 2022, **844**, 1–11.
12 Y. Liu, X. Wu, X. Guo, K. Lee, Q. Sun, X. Li, C. Zhang, Z. Wang, J. Hu, Y. Zhu, M. K. H. Leung and Z. Zhu, *Mater. Today Energy*, 2021, **19**, 1–8.
13 Y. Chen and A. El-Ghazaly, *Small*, 2023, **19**, 2205079.
14 G. Varvaro, D. Peddis, G. Barucca, P. Mengucci, V. Rodionova, K. Chichay, A. M. Testa, E. Agostinelli and S. Laureti, *ACS Appl. Mater. Interfaces*, 2015, **7**, 22341–22347.
15 B. Muzzi, M. Albino, C. Innocenti, M. Petrecca, B. Cortigiani, C. de, J. Fernández, G. Bertoni, R. Fernandez-Pacheco, A. Ibarra, C. Marquina, M. R. Ibarra and C. Sangregorio, *Nanoscale*, 2020, **12**, 14076–14086.
16 H. K. Daima, P. N. Navya, S. Ranjan, N. Dasgupta and E. Lichtfouse, *Nanosci. Med.*, 2020, **1**, 39.
17 J. Bai, Y. Xu, J. Thomas and J. Wang, *Nanotechnology*, 2007, **18**, 1–5.
18 G. Song, M. Kenney, Y. S. Chen, X. Zheng, Y. Deng, Z. Chen, S. X. Wang, S. S. Gambhir, H. Dai and J. Rao, *Nat. Biomed. Eng.*, 2020, **4**, 325–334.

19 J. M. D. Coey, *Magnetism and Magnetic Materials*, Cambridge University Press, 2001.
20 E. Fish, *Proc. IEEE*, 1990, **78**, 947–972.
21 T. Sourmail, *Prog. Mater. Sci.*, 2005, **50**, 816–880.
22 R. S. Sundar and S. C. Deevi, *Int. Mater. Rev.*, 2005, **50**, 157–192.
23 J. M. MacLaren, T. C. Schulthess, W. H. Butler, R. Sutton and M. McHenry, *J. Appl. Phys.*, 1999, **85**, 4833–4835.
24 B. D. Cullity and C. D. Graham, *Introduction to Magnetic Materials*, John Wiley & Sons, Inc., Hoboken, NJ, USA, 2008.
25 L. Leyssens, B. Vinck, C. Van Der Straeten, F. Wuyts and L. Maes, *Toxicology*, 2017, **17**, 1–54.
26 M. Lu, M. Liu, L. Wang, S. Xu, J. Zhao and H. Li, *J. Alloys Compd.*, 2017, **690**, 27–30.
27 S. Wu, A. Sun, Z. Lu, C. Cheng and X. Gao, *J. Magn. Magn. Mater.*, 2015, **381**, 451–456.
28 F. Casula, M. A. Corrias, A. Falqui, V. Serin, D. Gatteschi, C. Sangregorio, C. Fernandez and G. Battaglin, *Chem. Mater.*, 2003, **15**, 2201–2207.
29 A. K. Giri, C. De Julian and J. M. Gonzalez, *J. Appl. Phys.*, 1994, **76**, 6573–6575.
30 X. Lu, G. Liang and Y. Zhang, *Mater. Lett.*, 2007, **61**, 4928–4931.
31 P. Tartaj and C. J. Serna, *J. Am. Chem. Soc.*, 2003, **125**, 15754–15755.
32 H.-S. Cho, M. S. Noh, Y.-H. Kim, J. Namgung, K. Yoo, M.-S. Shin, C.-H. Yang, Y. J. Kim, S.-J. Yu, H. Chang, W. Y. Rho and B.-H. Jun, *Nanomaterials*, 2024, **14**, 268.
33 P. Sahu and M. Ali, *Mol. Syst. Des. Eng.*, 2022, **7**, 1501–1515.
34 C. Mohr, M. Dubiel and H. Hofmeister, *J. Phys.: Condens. Matter*, 2001, **13**, 525–536.
35 C. Briese, L. S. Selle, C. Patzig, Y. Hu, J. Deubener and T. Höche, *J. Non Cryst. Solids*, 2020, **549**, 1–9.
36 G. Ennas, A. Falqui, S. Marras and C. Sangregorio, *Chem. Mater.*, 2004, **16**, 5659–5663.
37 A. Casu, M. F. Casula, A. Corrias, A. Falqui, D. Loche, S. Marras and C. Sangregorio, *Phys. Chem. Chem. Phys.*, 2008, **10**, 1043–1052.
38 G. Concas, F. Congiu, G. Ennas, G. Piccaluga and G. Spano, *J. Non Cryst. Solids*, 2003, **330**, 234–241.
39 C. Cannas, A. Musinu, D. Peddis and G. Piccaluga, *Chem. Mater.*, 2006, **18**, 3835–3842.
40 G. Ennas, G. Marongiu, S. Marras and G. Piccaluga, *J. Nanopart. Res.*, 2004, **6**, 99–105.
41 A. Omelyanchik, G. Varvaro, P. Maltoni, V. Rodionova, J.-P. M. Murillo, F. Locardi, M. Ferretti, C. Sangregorio, F. Canepa, P. Chernavsky, N. Perov and D. Peddis, *Appl. Sci.*, 2022, **12**, 1899.
42 A. E. Danks, S. R. Hall and Z. Schnepp, *Mater. Horiz.*, 2016, **3**, 91–112.
43 C. Cannas, A. Musinu, D. Peddis and G. Piccaluga, *J. Nanopart. Res.*, 2004, **6**, 223–232.
44 S. E. Sandler, B. Fellows and O. T. Mefford, *Anal. Chem.*, 2019, **91**, 14159–14169.
45 C. Granados-Miralles, A. Quesada, M. Saura-Múzquiz, H. L. Andersen, J. F. Fernández and M. Christensen, *Mater. Chem. Front.*, 2020, **4**, 1222–1230.
46 H. Stuart and N. Ridley, *J. Phys. D: Appl. Phys.*, 1969, **2**, 302.
47 D. Bardos, *J. Appl. Phys.*, 1969, **40**, 53–55.
48 B. Hourahine, B. Aradi, V. Blum, F. Bonafé, A. Buccheri, C. Camacho, C. Cevallos, M. Y. Deshaye, T. Dumitrică, A. Dominguez, S. Ehlert, M. Elstner, T. van der Heide, J. Hermann, S. Irle, J. J. Kranz, C. Köhler, T. Kowalczyk, T. Kubař, I. S. Lee, V. Lutsker, R. J. Maurer, S. K. Min, I. Mitchell, C. Negre, T. A. Niehaus, A. M. N. Niklasson, A. J. Page, A. Pecchia, G. Penazzi, M. P. Persson, J. Řezáč, C. G. Sánchez, M. Sternberg, M. Stöhr, F. Stuckenberg, A. Tkatchenko, V. W. -Z. Yu and T. Frauenheim, *J. Chem. Phys.*, 2020, **152**, 124101.
49 G. Kresse and J. Furthmüller, *Phys. Rev. B*, 1996, **54**, 11169–11186.
50 N. Ntallis, D. Peddis and K. Trohidou, DFT calculations of high moment $Fe_{1-x}Co_x$ alloy and Fe/Co, Co/Fe core shell magnetic nanoparticles, 2025, RSC, in submission.
51 T. Block, N. Knoblauch and M. Schmücker, *Thermochim. Acta*, 2014, **577**, 25–32.
52 A. Omelyanchik, M. Salvador, F. D'Orazio, V. Mameli, C. Cannas, D. Fiorani, A. Musinu, M. Rivas, V. Rodionova, G. Varvaro and D. Peddis, *Nanomaterials*, 2020, **10**, 1288.
53 J. R. Porter, L. C. De Jonghe and D. Jonghe, *Metall. Trans. B*, 1981, **12**, 299–309.
54 A. Corrias, F. M. Casula, G. Ennas, S. Marras, G. Navarra and G. Mountjoy, *J. Phys. Chem. B*, 2003, **107**, 3030–3039.
55 T. Dippong, O. Cadar and E. A. Levei, *Materials*, 2022, **15**, 2996.

